

Manufacturing Letters

Manufacturing Letters 35 (2023) 184-193



51st SME North American Manufacturing Research Conference (NAMRC 51, 2023)

Biomimetic Hydrogel Scaffolds Embedded with Porous Microtubes as Perfusion Channels

Nan Zhang, Imtiaz Qavi, Sampa Halder, George Tan*

Department of Industrial, Manufacturing and Systems Engineering, Texas Tech University, Lubbock, TX 79409

* Corresponding author. Tel.: +1 806-834-3325 E-mail address: george.z.tan@ttu.edu

Abstract

Despite the remarkable progress in biofabrication, the vascularization of large-sized tissue scaffolds remains a great challenge for tissue engineering. The lack of effective capillary vessels in the scaffold can result in cellular necrosis due to the lack of oxygen and nutrients. Integrating capillary vessels in scaffolds is critical to maintaining cellular metabolic functions and the ultimate success of engineering large-scale tissues and organs. This paper demonstrates a novel hybrid biofabrication method that combines coaxial electrospinning and extrusion-based bioprinting to fabricate microtube-embedded hydrogel scaffolds. The porous microtubes mimicked the capillary morphology and were embedded between layers of 3D printed sodium alginate scaffold to function as a microchannel diffusion system. The dye diffusion test showed that the microtubes enhanced the mass transport within the scaffold.

© 2023 The Authors. Published by ELSEVIER Ltd. This is an open access article under the CC BY-NC-ND license (https://creativecommons.org/licenses/by-nc-nd/4.0)

Peer-review under responsibility of the Scientific Committee of the NAMRI/SME.

Keywords: Bioprinting, Electrospinning, Hybrid Manufacturing, Artificial Capillary Vessels, Tissue Engineering

1. Introduction

Tissue engineering, which aims to develop biological substitutes that replicate natural tissues to replace damaged tissues or organs [1], has witnessed remarkable progress in the past three decades. In general, cells are incorporated into a three-dimensional (3D) scaffold that has similar structures and functions to support cell proliferation, nutrition transportation, and oxygen exchange. Additive manufacturing technologies enable the rapid prototyping of cell/biomaterial matrices with accurate control over the 3D geometry. This interdisciplinary area of manufacturing engineering and tissue engineering is also known as bioprinting. A variety of bioprinting techniques have been developed for the fabrication of cell-laden 3D scaffolds, including stereolithography [2], cell sheet lamination [3], inkjet printing [4, 5], laser-assisted printing [6, 7], and extrusion-based printing [8, 9] among others. Compared with physicochemical biofabrication methods, such as solvent casting, lyophilization, and gas foaming, bioprinting requires less lead time and has high flexibility in material properties and

structures [10, 11]. However, one of the primary challenges in current tissue engineering is the vascularization in large-sized tissue scaffolds. In the human body, organs and tissues are sustained by the blood circulatory system, which comprises a network of blood vessels. While large arteries and veins are to transport blood, capillary vessels are the key channels to deliver nutrients and oxygen to cells in tissues. For most hydrogelbased bioprinted tissues, the lack of functioning capillaries in the scaffold is a major hurdle for upscaling the fabrication size [12, 13] because cells that are far from the medium-scaffold interface (over 200 µm) will eventually die due to the lack of oxygen and nutrient. Even a porous structure cannot guarantee an effective mass diffusion because of the structural deformation after the swelling. The integration of the perfusion channels as capillary vessels in the cell-laden scaffold to maintain cellular metabolic functions is the prerequisite for the success of engineering large-scale tissues and organs.

One possible solution to improve perfusion through thick tissues is to embed microfluidic networks to break the diffusion limit of hydrogels (~200 µm). Studies have shown that microfluidic channels can efficiently deliver nutrients to encapsulated cells and that there is a significant difference in cell viability between scaffolds with and without microfluidic channels [14, 15]. Several methods have been explored to engineer microchannel structures that mimic vascular networks. Seung-Schik Yoo et al. [14] used gelatin printed between layers of collagen, which was then liquefied and drained at 37°C to form hollow channels within the collagen scaffold. This method showed low cellular viability when the sacrificial material was removed. Du et al. [16] proposed a method for the rapid construction of cell-laden hydrogel structures containing cells embedded in vascular-like microchannels with circular lumens. Photolithography was used to create microgel arrays with predetermined internal microchannels, which were subsequently combined into 3D tubular constructions with multi-level interconnecting lumens. However, this method is cumbersome and difficult to be scaledup for centimeter-sized tissue scaffolds. To print tubular channels, Zhang et al. [17] combined cartilage cells with alginate-based bioinks. These printable microfluidic tubes, which resembled vessels, were able to transfer oxygen, nutrients, and biomolecules while also promoting cell development. In a related study, Gao et al. [18] reported a coaxial system that allows 3D printing of high-strength structures with microchannels for nutrient delivery using hydrogel. Freeform reversible embedding of suspended hydrogels (FRESH) 3D printing method has also been widely investigated for creating vascularization [19, 20]. However, these millimeter-sized channels are substantially larger than human capillaries by several orders of magnitude.

Our prior studies have demonstrated the feasibility of the rapid fabrication of porous microtubes with an average diameter of 5 microns [21-23]. In this research, we designed a hybrid bioprinting process to create capillary-embedded hydrogel scaffolds by combining extrusion bioprinting with core-sheath wet electrospinning. The concept is to integrate porous microtubes as artificial capillaries in a hydrogel scaffold to enhance internal mass diffusion. One obvious challenge in this conceptual design is the in-situ formation of microtubes without additional post-processing. We hypothesize that the core-sheath structured microfibers will form a porous tubular structure without deformation after the sodium alginate aqueous bioink dissolves the waster-soluble cores. To test this hypothesis, we investigated the effects of process parameters on the microtube morphology and the structural integration between the microtubes and the hydrogel. In addition, we evaluated the mass diffusion efficacy, elevated-pressure mass transport, and cellular viability of the 3D scaffolds with or without microtubes to validate the expected function of these artificial capillaries.

2. Materials and Methods

2.1. Preparation of hydrogel

To prove the concept, we used sodium alginate as the hydrogel for its proven biocompatibility and printability [24,

25]. It has been widely used for in vivo and in vitro tissue engineering studies [25]. The sodium alginate (SA) was purchased from Research Products International (Illinois, USA). The SA aqueous solution was prepared by mixing SA powders in deionized (DI) water with an overhead stirrer at room temperature for 30 minutes. We tested SA aqueous solutions with different concentrations in a pilot study and determined 6% (w/v) SA aqueous solution for the bioprinting process due to its proper rheology property for printability. 4% (w/v) calcium chloride solution was prepared by a magnetic stirrer. The solution was stirred for 5 minutes in a 100 mL beaker at room temperature. This solution concentration is suitable for crosslinking the SA structure via the process of calcium-sodium ion exchange [26]

2.2. Preparation of Electrospinning solutions

Polycaprolactone (PCL, MW = 80,000, Sigma-Aldrich, St. Louis, MO) was dissolved in Dichloromethane (DCM) at a concentration of 12% (w/v) to prepare the shell electrospinning solution. Polyethylene oxide (PEO, MW = 300,000, Sigma-Aldrich, St. Louis, MO) was mixed in DCM at a concentration of 6% (w/v) as the core solution. PCL and PEO are biocompatible and biodegradable [27-30]. The solutions were stirred on a magnetic stirrer for 4 hours at room temperature. The mass change due to the DCM evaporation was measured by a precision balance. The loss of solvent was compensated daily by adding the proper amount of DCM by weight.

2.3. Preparation of dye solutions

Cell-tracker CM-DI (ThermoFisher) pink was used to study the permeability of the microtubes in the hydrogel scaffold. A small volume of 100 μL of the pure dye was pipetted into 100 mL of DI water. The resultant solution created a fluorescent (I = 425) red image under the laser excitation ($\lambda = 510$ nm). The intensity of the fluorescent image is proportional to the mass of the dye. Therefore, the color gradient visualizes the mass diffusion in a given space.

2.4. Viscosity measurements

The rheological properties of the bioprinting and electrospinning solutions were measured using an MCR 92 Modular Compact Rheometer (Anton Paar, Austria). The samples were subjected to rotational viscoelastic measurements using a 25 mm-diameter rotating flat plate. The shear stress was set from 0.1 to 1000/s range, and the corresponding viscosity values were calculated. In each case, 1.5 mL of the solution was used from the prepared stock solutions.

2.5. Surface Tension measurement

The surface tensions of the bioprinting and electrospinning solutions were measured using the Theta-Lite (Biolin Scientific, Sweden). The equipment operates by analyzing the shape/size parameters of a pendent droplet of the test liquid sample to obtain the surface tension of the liquid-air interface.

In each case, the droplet was allowed to grow up to $4.5~\mu L$ in volume to reach the calibrated standard for the measurement process. Once the target volume was reached, the shadowgraph camera system started recording images at 24 frames per second (FPS) for a total of 1 minute. This resulted in approximately ~1400 sample data points for the surface tension values, which were sufficient for getting the normal and standard deviation values for each sample measurement.

2.6. Bioprinting and Electrospinning

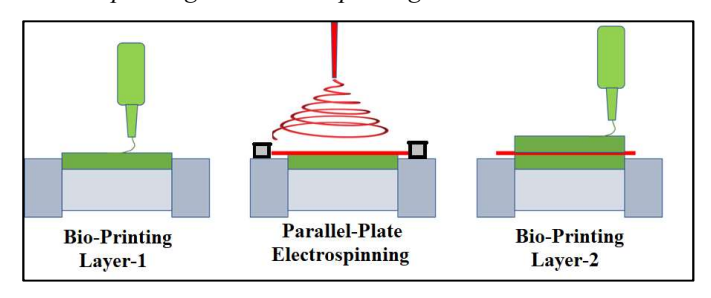


Fig. 1. The electrospinning-assisted hybrid bioprinting process.

We printed 2×2 cm SA samples using a Cellink+ (San Carlos, CA) bioprinter through a 25G nozzle with a pneumatic pressure of 90-95 KPa. The scaffold comprised four layers with a total thickness of 0.5 cm.

We prepared hydrogel scaffolds with or without microtubes. The steps involved in the hybrid fabrication process are shown in Figure 1. CaCl₂ was sprayed onto the first two layers of SA before printing the subsequent two layers. The $CaCl_2$ between the two halves allowed a partial crosslinking of the scaffold to prevent uneven crosslinking and swelling that lead to deformation of the scaffold. To incorporate microtubes into the SA scaffold, porous PCL/PEO microfibers were deposited on the first half of the SA scaffold through the wet core/sheath electrospinning. The electrospinning was carried out with flow rates of 1.5 and 2.4 ml/hr for the core and the sheath solution, respectively. The spinning distance was set to 10 cm with an applied voltage of 8 kV. Two parallel aluminum bars were used as the collector to generate aligned microtubes. The alignment of microtubes would minimize the total length of the microtubes needed to perfuse liquid in the hydrogel, therefore, enhancing transportation efficiency. The relative humidity (RH) in the system was maintained over 65% to allow surface pore formation on the microtube walls. The CaCl₂ spray dissolved the PEO cores to form the microtubes. Afterward, the bioprinter resumed the SA printing on the top of the microtubes and completed the scaffold. After printing, the whole scaffold was placed in the $CaCl_2$ bath for a complete crosslinking.

2.7. Dye diffusion Test

We hypothesized that the microtubes would improve mass diffusion within the hydrogel structures. To test this hypothesis, we designed a hydrogel structure with microtubes extended from the hydrogel boundary. The extended microtubes served as transport channels for diffusion. A scaffold without microtubes served as the control group. Both types of scaffolds were submerged in a water bath (50 ml)

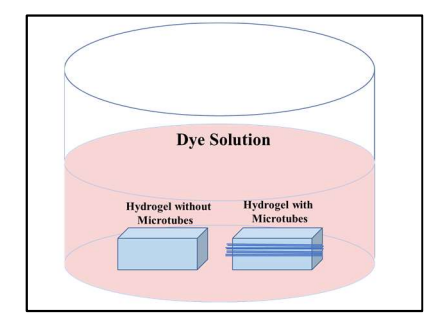


Fig. 2. Setup of the dye diffusion test

containing the CM-DI red dye (concentration = $0.1\% \ v/v$) for approximately two hours to allow the diffusion of dye into the hydrogel. The submersion was performed after the crosslinking by CaCl2. It is to be noted that no external pressure gradient was applied to allow liquid flow into the hydrogel structure. Only the natural diffusion through the microtubes was investigated. The process is shown in Figure 2.

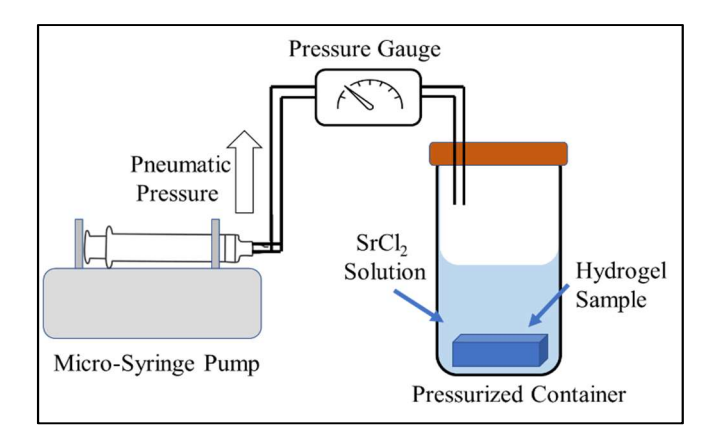


Fig. 3. Setup of the elevated-pressure mass transport test

2.8. Elevated pressure mass transport test

In order to investigate the mass transportation capability of the produced microtubes within the hydrogel scaffold, we conducted an elevated-pressure test. Since our sample already contains sodium and calcium ions, we used strontium as an indicator element. The hydrogel sample was taken into a sealed pressure container containing 25 mL of strontium chloride solution. A micro-flow syringe pump (Cole-Palmar, Illinois) was used to generate the pneumatic pressure. A pressure equivalent to 1.15 atm (120 mm Hg gauge pressure) was generated to mimic the systolic blood pressure in the human body. The samples were kept in the pressurized container for a total of 30 minutes. The setup used for the elevated pressure mass transport test is shown in Figure 3.

2.9. Freeze drying and sample imaging

To examine the microstructure of the hybrid scaffold under the scanning electron microscope, we first placed the microtube-embedded SA scaffold in a cryogenic freezer (ThermoFisher) at -80°C for 24 hours then lyophilized the scaffold at 1 mPa and -45 °C in a 2.5L freeze-dryer (Labconoco, MO) for 48 hours. Afterward, the lyophilized scaffold was submerged in liquid nitrogen for 3 minutes for cryo-sectioning.

The cryo-sectioning allows the sample to be cut along the cross-section plane of the microtubes. The cross-sectioned samples were vacuum sputtered with a gold coating and then examined under the scanning electron microscope (SEM). All the SEM images were acquired at 10 kV accelerating voltage using a secondary electron detector (SED). We used the Zeiss Crossbeam 540 FIB-SEM and Phenom Pro-X desktop for the energy dispersive x-ray spectrometry (EDS) and back-scatter electron detection (BSD), respectively, in the elevated pressure mass transport test. The preparation for the SEM imaging is illustrated in Figure 4.

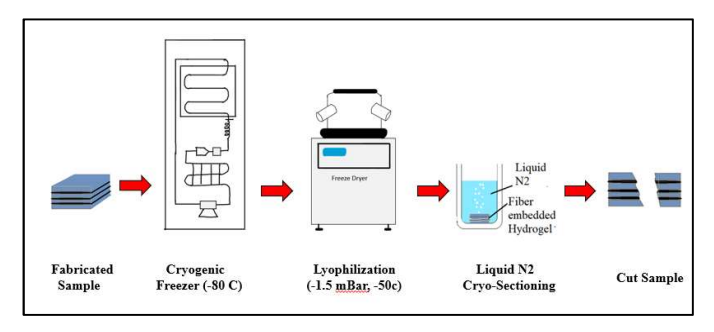


Fig. 4. Process of preparing the samples for the SEM imaging.

2.10. Cell Culture and viability test

GFP-expressing human primary dermal microvascular endothelial cells were purchased from (Cell Biologics, Inc., Chicago, IL). Cells were thawed, centrifuged, and resuspended in endothelial cell base medium (Cell Biologics, Inc., Chicago, IL) with 10% fetal bovine serum (FBS, Avantor Seradigm, Radnor, PA) and 0.1 mg/ml ampicillin (Santa Cruz Biotechnology, Dallas, TX). The cells were cultured in a 75 cm² flask at 37 °C and 5% CO2 for 10 days to reach 80% confluency. The bioink was prepared by mixing sodium alginate in the complete endothelial cell medium as described in section 2.1. The cells were then detached and added into the bioink at a concentration of 10,000 cells/ml. The cell viability was accessed using Biotium 30002-T assay (Fremont, CA). The live and dead cells were imaged using an EVOS FL (Thermo-Fisher, Waltham, MA).

3. Results and Discussion

3.1. Viscosity and Surface Tension

Fluidic properties of the working solutions are critical in both electrospinning and bioprinting. The viscosities of the 12% (w/v) PCL-DCM, 6% (w/v) PEO-DCM, and 6% (w/v) SA aqueous solution are presented in Figure 5. We used the Carreau-Yasuda regression model for determining the complex viscosities as a function of the shear rate, which is given by the following equation [31, 32]:

$$\eta(\gamma) = \mu^{\infty} + (\mu_0 - \mu^{\infty})[1 + (\gamma \lambda^a)^{(n-1)/a}] \dots$$
 (Equation 1)

where,

 γ = shear rate

 $\eta(\gamma)$ = viscosity at specified shear rate (γ)

 μ^{∞} = viscosity at infinite shear rate

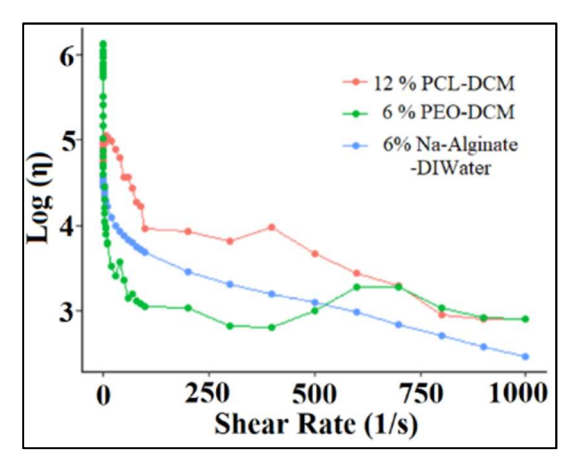


Fig. 5. Summary of the viscosity of the solutions

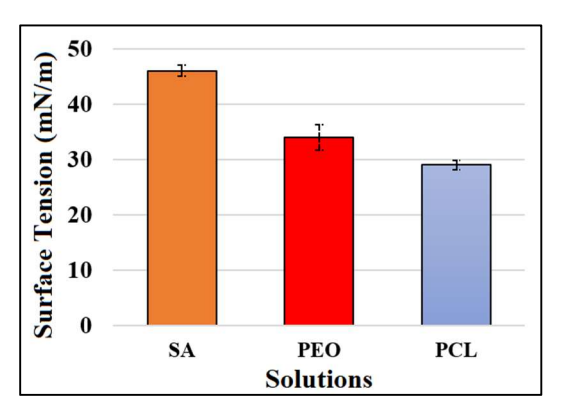


Fig. 6. Summary of the surface tension of the solutions

 μ_0 = viscosity at rest condition

 λ = relaxation time

a, n = dimensionless material-specific coefficients

Electrospinning jets are subjected to high air-fluid boundary shear forces upon their jetting from the Taylor Cone. For the electrospinning solution, we compare the viscosity values at high shear rates of 1000/s based on previous literature [33]. From equation (1), the obtained viscosities at the shear rate of 1000/s for the PCL and PEO were approximately 800 Pa·s. For the hydrogel solution, we were more interested in the zeroshear viscosity. This is because the high zero-shear viscosity is desirable for holding the structural shape of hydrogels. From our equation (1), the obtained value of the zero-shear viscosity or resting viscosity for the 6% (w/v) SA solution is approximately 301 Pa·s. Previous studies suggested using resting viscosities within a range of 3-300 Pa·s for bioprinting applications [34]. Hence, we are at the borderline of the upper critical limit with our current solution. Overall, all the solutions showed a shear-thinning property.

The result of the surface tension test is shown in Figure 6. The hydrogel structure has the highest surface tension value at 46 mN/m compared to the electrospinning solutions. The surface tensions of DI water and DCM were 72 and 29 dynes/cm, respectively. The surface tension is important to the overall line-to-line spread of the hydrogel during the bioprinting process. Therefore, we expect sufficient surface tension forces to restrain gel spreading [35].

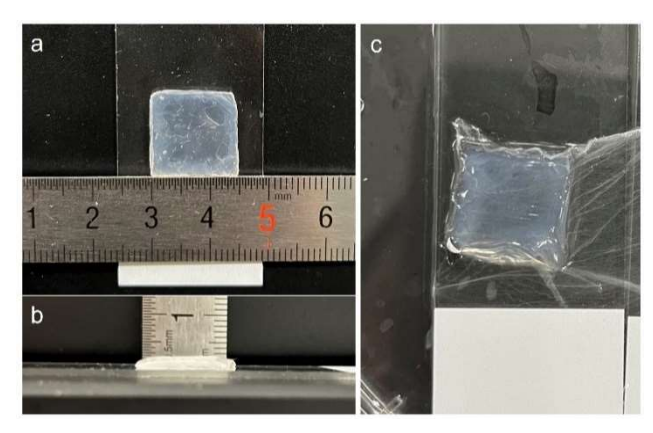


Fig. 7. (a) A top view of the shrunken hydrogel scaffold after the crosslinking. The actual width is 15 mm. (b) A side view of the hydrogel scaffold. The actual thickness is 2.5 mm. (c) A hydrogel scaffold embedded with aligned microtubes.

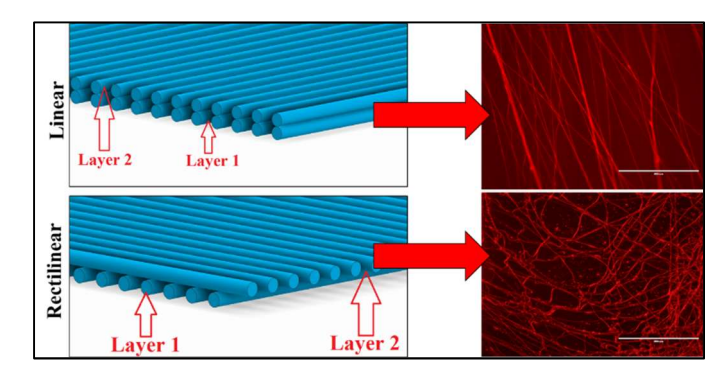


Fig. 8. The effect of bioprinting pattern on the microtube orientation. Scale bar = $400 \mu m$

3.2. Effect of printing pattern on fiber orientation

Figure 7 shows the printed acellular hydrogel scaffolds with and without microtubes. After the crosslinking, the hydrogel shrunk by approximately 25%. The microtube mesh did not affect the geometry integrity of the hydrogel scaffold.

Because the microtubes were aligned on the bottom half of the SA scaffold, the infill pattern of the upper half would influence the microtube orientation. As shown in Figure 8, when the printing direction of the upper layer was perpendicular to the lower layer, the printing nozzle tended to drag the deposited microtubes and eventually led to a random microtube network. Even after adding enough clearance between the nozzle and deposition layers, the dragging effect was still observed, because the momentum from the nozzle was transferred through the highly viscous SA extrudate to the microtubes. To mitigate the dragging effect on the microtube alignment, we changed the infill orientation to be the same as the microtube orientation. With this modification, the microtubes maintained the alignment in the scaffold.

3.3. Microstructure of the hydrogel scaffold with microtubes

Microtube formation from the core/sheath electrospinning process requires the dissolution of the PEO core. The morphology of the microtubes was inspected under the SEM. Figure 9 (a and b) show that microtubes with well-defined

tubular structure and surface pores formed due to the vapor induced phase separation.

Figure 10 shows the microtubes embedded within the freeze-dried hydrogel scaffold. The last image shows the formation of a well-defined microtube-like structure formed within the hydrogel structure. The outside diameter of the microtubes were within 5-10 μ m, which mimics the scale of the human capillary blood vessels.

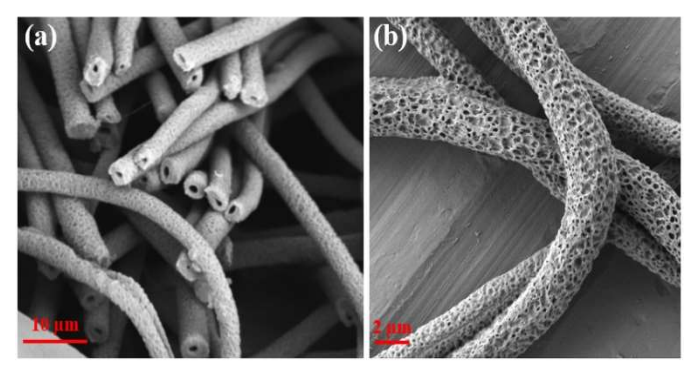


Fig. 9. SEM images of (a) microtubes (b) nanopores on the surface of the microtubes

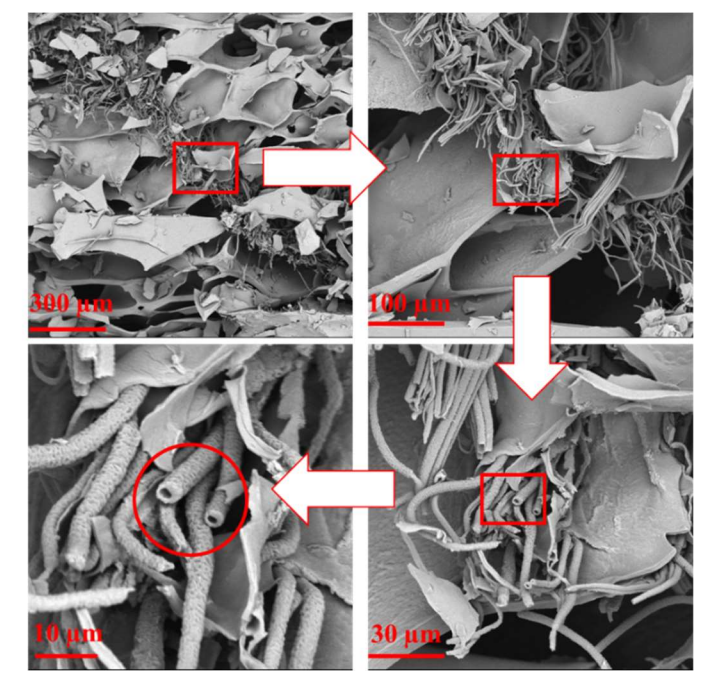


Fig. 10. Sequential images showing the embedded microtubes within the hydrogel scaffold.

3.4. Dye absorption in hydrogel visualized using fluorescence microscopy

The amount of dye absorbed within the hydrogel structures was quantified by the fluorescence intensity measurement. ImageJ was used to analyze the fluorescence intensity of the obtained images. The original image was color-split using the Red-Green-Blue (RGB) splitter. This splits the three basic colors (Red, Green, and Blue) in a digital image into three separate channels. Each pixel in the channel was assigned a numerical intensity value between $0 \le I \le 255$, depending on its particular basic color intensity.

Based on the intensity value, the pixels either appeared white (I = 255), dark (I = 0), or grey ($0 \le I \le 255$). Hence the images in each RGB-split channel appear greyscale. Ten individual grid boxes with regions of interest (ROI) measuring 700x50 µm (Mid-Layer) and 700x100 µm (Top-Layer) were stacked next to each other to quantify the fluorescence intensity in those ROIs. The ROIs were different for the two layers owing to the difference in their original captured image magnification and scale. The boxes were taken in longitudinal shape to measure the fluorescence intensity change from the edge to the interior of the hydrogel. The intensity values were then plotted as bars corresponding to each grid position box in the hydrogel with or without microtubes from 3 different sample zones (n=3 for each ROI).

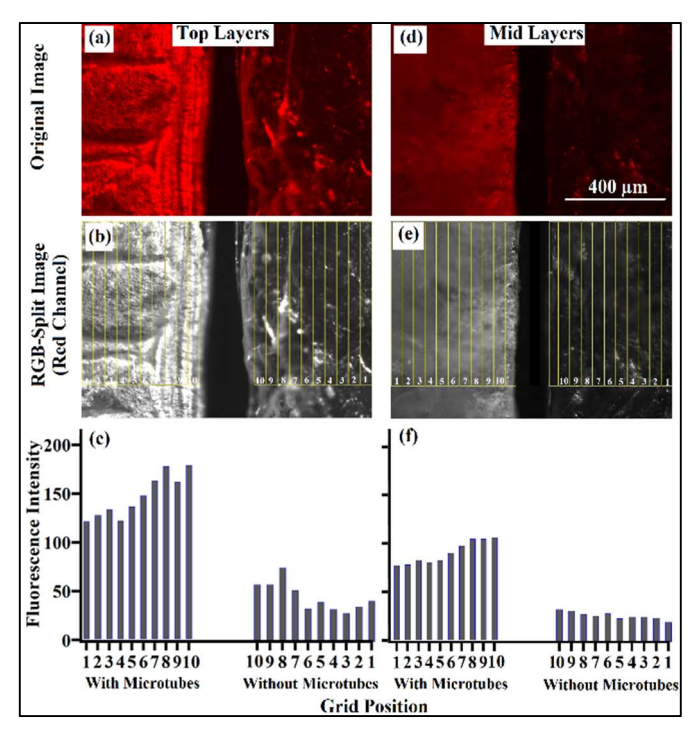


Fig. 11. Comparison of the fluorescence intensity of hydrogels with and without microtubes. (a) Original fluorescence image of top layers. (b) Red colour channel from RGB-split with intensity measurement grids for top layers. (c) The average intensity values aligned with grid positions for the top layers. (d) Original fluorescence image of the mid/intermediate layers. (e) Red colour channel from RGB-split with intensity measurement grids for the mid layers. (f) The average intensity values aligned with the grid positions for the mid-layers.

Figure 11 shows the fluorescence intensity measurement for the top and middle layers of hydrogels with or without microtubes. Images 11(a,d) show the raw fluorescence top and middle layers, respectively. Figures 11b-e show the RGB-split greyscale images with the ROIs highlighted. Figures 11(c, f) show the intensity measurements for each ROI position aligned with images 11(b,e). The top layer of the hydrogel with microtubes has intensity values between 120 to 160. For the top-layer without the microtubes, the intensity values were between 30 and 75. For both types of hydrogels, the intensity decreased as the distance from the edge increased. The decreasing gradient of fluorescence intensity in the hydrogel with microtubes shows that the microtubes did play a role in the mass transportation of the dye molecules from the edge to the interior section.

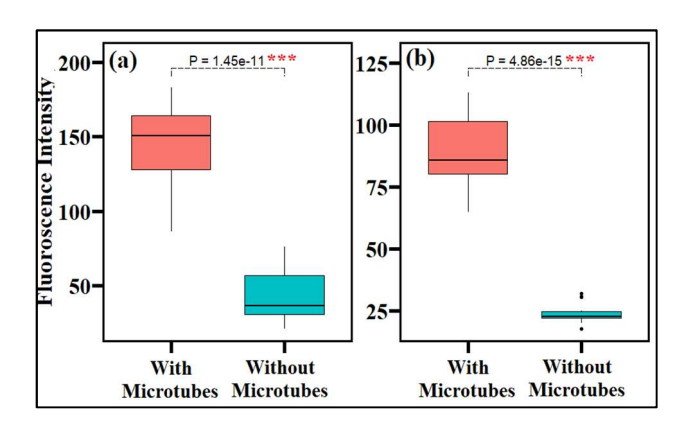


Fig. 12. Boxplot with the Wilcoxon Test p-value for hydrogels with or without microtubes in the (a) top layer (b) mid layer.

The mid-layers of the hydrogels also show similar trends with and without microtubes. The reduction in fluorescence intensity from the top to the middle layer was attributed to the fewer exposure areas to the fluorescence dye.

To quantitative evaluate the fluorescence intensity in the hydrogels with and without microtube, we randomly sampled a total of 10 data points per image from 3 fluorescence images (n = 30) using a ROI of $100x100~\mu m$. The data showed that the variances between groups were not equal and did not follow a normal distribution. Hence we conducted a non-parametric test to calculate the level of significance. Figure 12 shows the boxplot comparison with the significance levels computed using the Wilcoxon Test (alpha = 0.05). Results showed that the fluorescence intensity in the hydrogel with microtubes significantly differed (P << 0.05) from that of hydrogel without microtubes (Figure 12 ab). This result confirmed that the electrospun microtubes enhanced the mass diffusion inside the hydrogel scaffold.

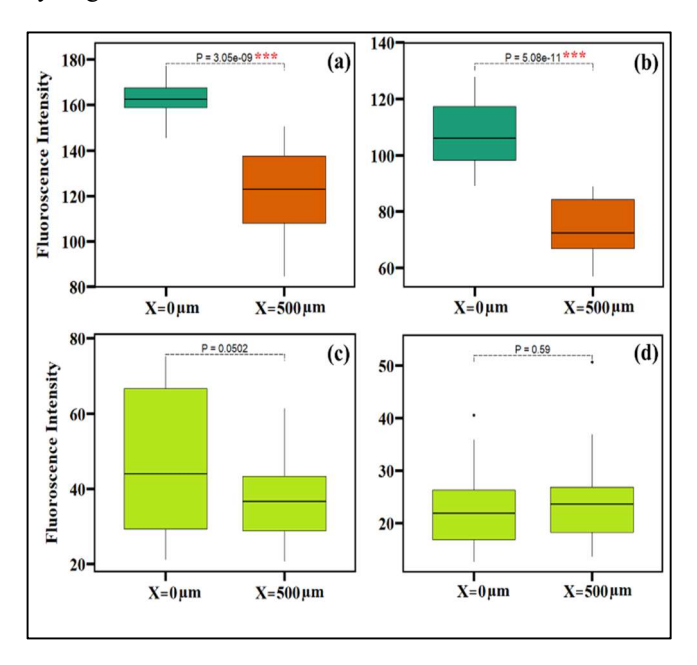


Fig. 13. Boxplot comparison of fluorescence intensity at the hydrogel edge ($x = 0 \mu m$) and $x = 500 \mu m$ from the edge- (a) top-layer with microtubes (b) intermediate layer with microtubes (c) top-layer without microtubes (d) intermediate layer without microtubes. Different colored boxes indicate statistically significant difference.

We then investigated the diffusion intensity along the length of the fiber orientation within the hydrogel. The intensity was measured using 50x50 μm ROI grids from the edge of the outer edge of the sample marked by $X = 0 \mu m$ and $X = 500 \mu m$ away from the edge of the hydrogel. A total of 20 individual data measurement ROI (n = 20) were taken from each group. Nonparametric Wilcoxon test (unequal variance between groups and non-normal data distribution) was conducted with alpha = 0.05. The results are plotted in Figure 13. The fluorescence intensity significantly changed (P<<0.05) along the microtubes in the hydrogel, suggesting that the dye diffusion took place through the microtubes. On the contrary, there was no locationdependent change of fluorescence intensity in the hydrogels without the microtubes (Figure 13cd). The quantitative analysis further confirmed the static diffusion of mass via the microtubes over an extended period of 3 hours.

3.5. The mass-transport capability of the microtubes at elevated pressure levels

We further investigated the accelerated mass transport of the microtubes in a pressurized bioreactor (1.15 atm). In this experiment, we used strontium (Sr), which has a high atomic number, as the indicator element for easy detection by the backscatter-electron detector (BSD) in the SEM. Hydrogel scaffolds $(2\times2\times1 \text{ cm})$ with and without microtubes were put in a test tube containing 3% (w/v) SrCl₂ solution. A single layer of microtubes was placed at the center (5 mm from top and bottom) of each hydrogel. We used an in-house built pneumatic micropump to generate approximately 120 mm Hg pressure in the solution containing our samples. The pressure was chosen to mimic the natural systolic pressure in the human circulatory system. The samples were kept under the micro-pressure environment for approximately 30 minutes, after which they were removed and processed for SEM imaging. The SEM and EDS characterization were performed using a Zeiss Crossbeam 540 FIB-SEM and Phenom Pro-X desktop, respectively.

Figure 14 shows the micro-analysis results of the hydrogel structure with the microtubes. The samples were broken down and laid flat on carbon tapes (Figure 14a) to reduce the charging effect at 15 kV needed for the electron dispersive x-ray spectrometry (EDS) analysis. The areas with brighter contrast in Figure 14a show the Sr precipitation in the hydrogel. Under the BSD imaging mode, heavier elements (higher atomic number) appear brighter owing to higher inelastic electron collisions [36]. Figure 14b shows the characteristic EDS peaks of an area with high salt precipitation (spectrum-1), and Figure 14c shows the peak of the dried hydrogel background. Due to the ion-exchange property of alginate, Sr²⁺ ions were expected in the background [37]. The Sr precipitation was also observed along the microtubes with the SEM-BSD imaging (Figure 14d) and further verified by EDS analysis (Figure 14e), showing that the microtubes transported the SrCl₂ solution into the hydrogel under pressure. Figure 15 shows the EDS mapping of Sr in the hydrogel. The Sr distribution was not homogenous. The precipitation of Sr is positively correlated with the proximity to the microtubes.

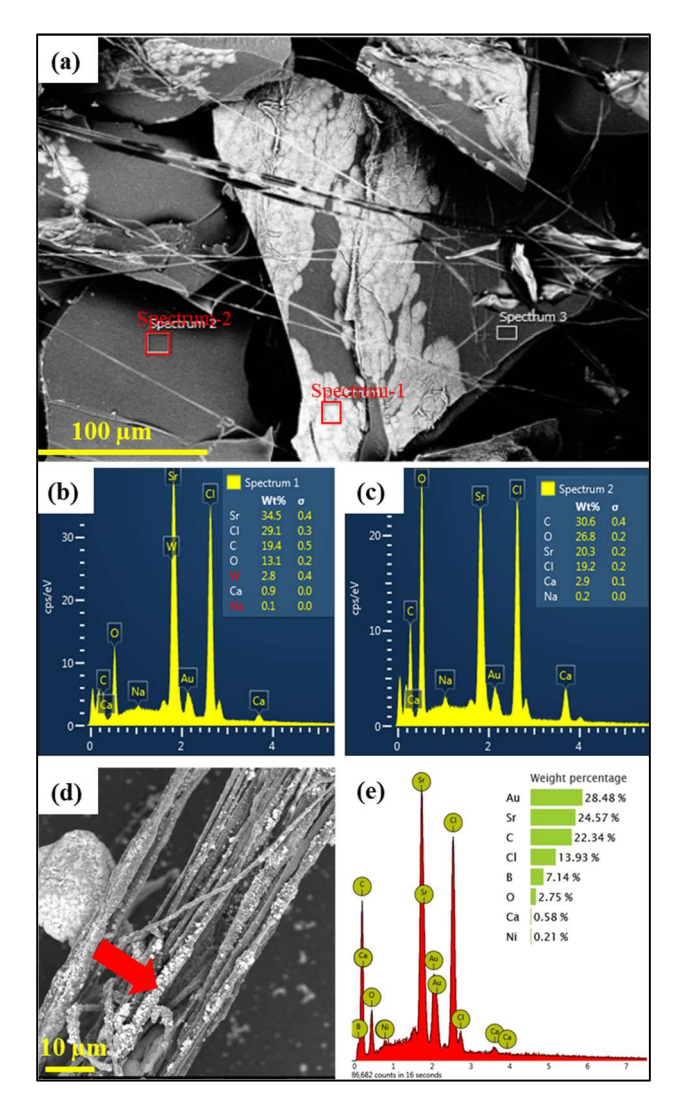


Fig. 14. (a) SEM-BSD micrograph of a 2x2x1 cm freeze dried hydrogel sample with microtubes (b) EDS characteristics peak of the salt precipitate zone (spectrum-1) (c) EDS characteristics peak of the dried hydrogel background (spectrum-2). (d) SEM-BSD imaging of the microtubes; salt precipitates (white-contrast) indicated by the red arrow (e) EDS characteristics peaks of the microtubes.

Figure 16(a-c) shows the SEM-BSD imaging of the central area of the hydrogel scaffold with the microtubes. The SrCl₂ precipitation was shown by the lighter contrast (marked by yellow arrows). The hydrogel without microtubes had almost no Sr precipitation (Figure 16df). Quantitative analysis was performed to evaluate the concentration of Sr atoms in the backgrounds of these images. A total of five data samples were taken (n = 5) to quantify the Sr atomic composition in different regions of the samples. Figure 16f shows a bar plot data distribution of Sr atomic composition percentage. The other atoms present in the sample were Na, Ca, Cl, C, and Au. Elements < 1% were considered noises.

We performed the Analysis of Variance (ANOVA) followed by the Tukey post hoc test. The significantly different groups with their respective P-values were marked in Figure 16g. Results show that the background hydrogel microstructure with and without microtubes had an almost similar composition of Sr due to the ion exchange process. The percentage of Sr in the precipitation zone significantly differed from the

background. Hence, we conclude that the microtubes acted as mass transport conduits that delivered fluids and ions into the center of a hydrogel scaffold at a pressure of 120 mm Hg that mimics the human systolic pressure.

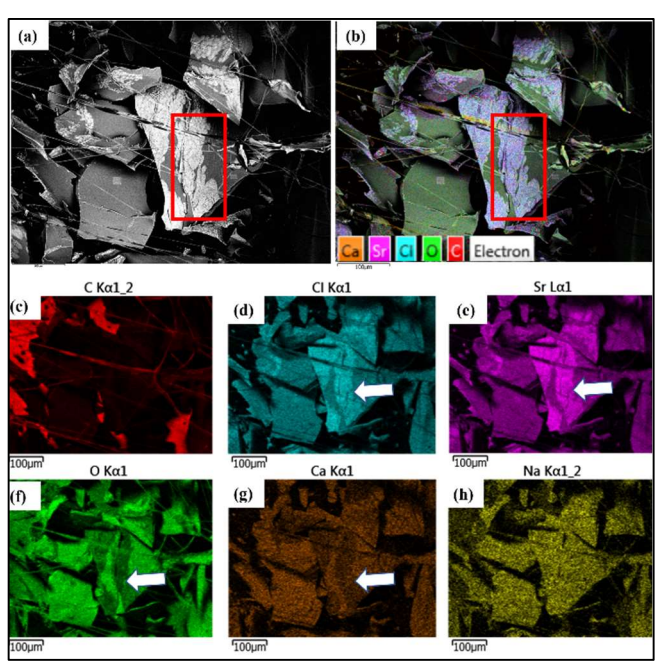


Fig. 15. (a) SEM-BSD micrograph of the freeze-dried sample (b) EDS element-stacked image of the sample with the red box showing the precipitation zone of interest. The EDS mapping of (c) carbon (d) chlorine (e) strontium (f) oxygen (g) calcium and (h) sodium. White arrows show the precipitation zones of interest.

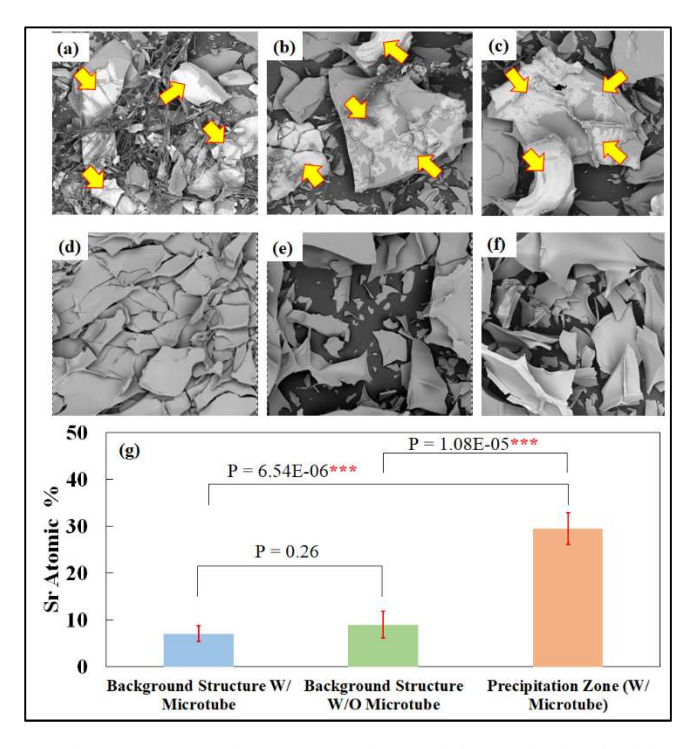


Fig. 16. Representative SEM-BSD images of the (a-c) hydrogels with microtubes and (d-f) without microtubes. Yellow arrows indicate the precipitation zones in the hydrogel sample with microtubes. (g) The percentage of Sr atom in different areas of the hydrogel.

3.6. Cell viability test

Figure 17 shows the green fluorescent endothelial cells in the microtube embedded hydrogel scaffold. The microtubes are biocompatible with human endothelial cells. The in-situ formation of microtubes in the hydrogel did not have any negative impact on cell viability. After three days of culturing, some cells attached to the microtubes and grew along the microtubes, forming either a linear or a branched structure that closely resembles the capillary vessels. The aligned microtubes acted as an attachment surface for the cells proximal to it and aided their growth along the microtubes.

Figure 18 shows the results for the cellular viability conducted with 2×2×1 cm hydrogel samples with and without microtubes. The cells were cultured in the hydrogel scaffolds for a total of 4 days before they were stained by the live-dead stains. Figures 18a and 18b show the live and dead cells in the hydrogels without and with microtubes, respectively. Data analysis was conducted using images at seven locations at the center of the hydrogels (n = 7), which were about 400 μ m away from the hydrogel-growth medium interface. The data showed normality (from Q-Q Plot), equal variance (from Leven's test) for different groups, and a large effect size (Cohen's d > 0.8). All of the tests met the criteria for a t-test with equal variance. Hence, we conducted a t-test to compare the cell density and viability in the hydrogel scaffolds with and without microtubes. Figure 18c shows a significant difference with P << 0.01 in the cell viability between hydrogel scaffolds with and without microtubes. In fact, the microtubes enhanced the cell viability from less than 15% to approximately 62%. The cell density (both alive and dead) was similar (p > 0.05) in both the hydrogel scaffolds (control and test group), suggesting the equivalent level of initial cell density in the hydrogel.

4. Discussion

The concept of fabricating micro/nano fiber-hydrogel composite structures has been explored in the past for various kinds of applications. From wound healing [38], drug delivery [39, 40] to cellular support and guidance structure [41, 42], to rolled nanofibers embedded in hydrogels forming coronary artery bypass grafts [43] have shown promising results. Different methods, such as the lamination technique, have allowed the pre-fabricated layers with different fiber angular orientations to be embedded in the hydrogel with cells growing along the fiber orientation directions [44]. One obvious challenge with such a technique is the possibility of crosscontamination due to the separated fabrication of fiber layers and hydrogel structures. Also, fabrication time and throughput for rapid fabrication become an issue. UV-curable hydrogels embedded with fibers were also proved to provide better structural control over fiber positioning owing to immediate photocurable crosslinking [45]. However, the UV poses a risk to the cell viability during the printing. To the best of our knowledge, this paper presents the first study of bioprinting hydrogel scaffolds with porous microtubes. This hybrid approach is expected to facilitate mass transport and induce vascularization in large-sized hydrogel scaffolds.

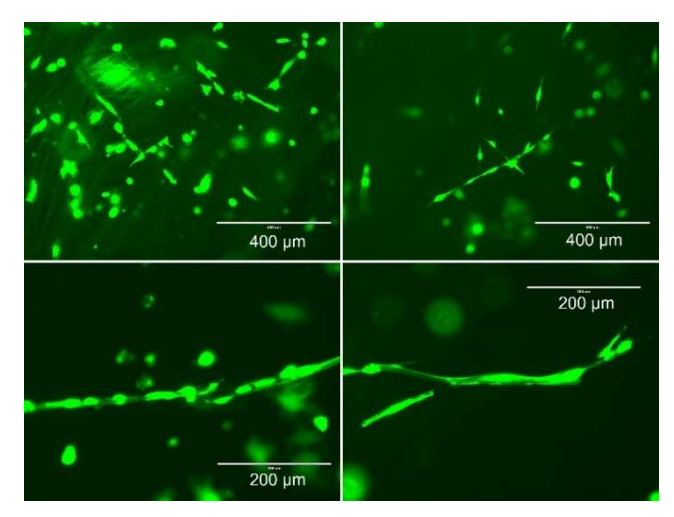


Fig. 17. GFP endothelial cells attached on the microtubes.

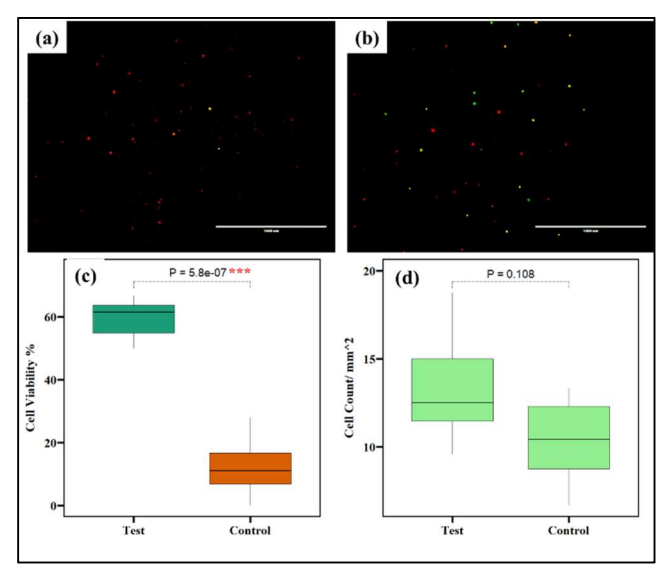


Fig. 18. Fluorescence imaging showing (a) hydrogel sample with microtubes (b) hydrogel samples without microtubes. The live and dead cells are marked by green and red stains respectively. Statistical comparisons of (c) cellular viability and (d) cell density. Scale bar = 1000 μm. Different colored boxplots indicate significant difference.

Alginate is a popular material which is widely used in 3D bioprinting. It behaves well in cartilage development, and it is also reported to be frequently used in other tissue development such as endothelial cells [46, 47], fibroblasts [18, 48, 49], and liver tissues [50], etc. For instance, Khalil and Sun [46] encapsulated endothelial cells inside alginate and 3D bioprinted the bioink into porous cell-laden constructs. They obtained high cell viability after bioprinting. Based on the positive results of previous research, we chose to use alginate as the bioink for endothelial cells. As a part of the future plan, a wide range of scaffold materials will be investigated.

There are several challenges in the current study. The non-uniform swelling of the hydrogel caused structural deformation of the scaffold. This could potentially affect the positioning of the microtubes within the scaffold and compromise the perfusion efficacy. The dye diffusion rate under static pressure conditions was quantified in the short interval range of 500 μm from the edge. In the future, we plan to look deeper into the

sample region to develop a mathematical correlation between various factors that influence the time-dependent diffusion rate through the microtubes. In addition, we plan to use confocal microscopy to study the diffusion efficacy of the microtubes.

Previous studies have already confirmed that electrospun nanofibers in hydrogel improved the mechanical properties of the scaffolds, e.g., tensile strength, toughness, and stiffness [51-53]. Moreover, prior studies show that polycaprolactone nanofibers can form a tightly packed network with the alginate microstructure [54]. The interfacial bonding can be further improved by reducing the hydrophobicity of the PCL polymer [55-58]. In the future, we plan to evaluate the effects of microtubes on the mechanical properties of the embedded scaffold. Furthermore, we will study the effect of microtubes on angiogenesis and test whether the microtubes can induce endothelial growth and migration into a network of capillary vessels in large hydrogel scaffolds (several to tens of centimeters).

5. Conclusion

This paper presented a hybrid fabrication technique for embedding microtubes in a hydrogel scaffold for tissue engineering. Core/sheath electrospinning into a bioprinted hydrogel scaffold resulted in porous microtubes that are morphologically similar to human capillary vessels. The wall of the microtubes also showed adequate structural integrity without being crushed by the liquid pressure following core dissolution. Critical bioprinting-related parameters, including solution viscosity and infill pattern, were adjusted to enhance the scaffold integrity and microtube orientation. The static dye diffusion and pressurized diffusion tests showed that the microtubes functioned as capillary vessels for improving mass transport, which was essential for tissue viability. The microtubes also significantly improved cell viability by the diffusion of vital nutrients into the center of a 4 cm³ hydrogel scaffold. Future studies will focus on cell proliferation and vascularization in the microtube-embedded hydrogel scaffolds for volumetric tissue engineering.

Acknowledgments

This work was supported by the National Science Foundation under grant number CMMI-2145108.

References

- [1] Vacanti, J.P. and R. Langer, *Tissue engineering: the design and fabrication of living replacement devices for surgical reconstruction and transplantation.* The lancet, 1999. **354**: p. S32-S34.
- [2] Das, S., et al., Bioprintable, cell-laden silk fibroin–gelatin hydrogel supporting multilineage differentiation of stem cells for fabrication of three-dimensional tissue constructs. Acta biomaterialia, 2015. 11: p. 233-246
- [3] Szymczyk-Ziółkowska, P., et al., A review of fabrication polymer scaffolds for biomedical applications using additive manufacturing techniques. Biocybernetics and Biomedical Engineering, 2020. 40(2): p. 624-638.
- [4] Boland, T., et al., Application of inkjet printing to tissue engineering. Biotechnology Journal: Healthcare Nutrition Technology, 2006. 1(9): p. 910-917.
- [5] Tse, C.C.W. and P.J. Smith, Inkjet printing for biomedical applications, in Cell-Based Microarrays. 2018, Springer. p. 107-117.

- [6] Ringeisen, B.R., et al., Laser printing of pluripotent embryonal carcinoma cells. Tissue engineering, 2004. 10(3-4): p. 483-491.
- [7] Schiele, N.R., et al., Laser-based direct-write techniques for cell printing. Biofabrication, 2010. 2(3): p. 032001.
- [8] Pati, F., et al., Extrusion bioprinting, in Essentials of 3D biofabrication and translation. 2015, Elsevier. p. 123-152.
- [9] Zhang, Y.S., et al., 3D extrusion bioprinting. Nature Reviews Methods Primers, 2021. 1(1): p. 1-20.
- [10] Mironov, V., et al., Organ printing: promises and challenges. 2008.
- [11] Nakamura, M., et al., *Biomatrices and biomaterials for future developments of bioprinting and biofabrication*. Biofabrication, 2010. **2**(1): p. 014110.
- [12] Ozbolat, I.T. and Y. Yu, Bioprinting toward organ fabrication: challenges and future trends. IEEE Transactions on Biomedical Engineering, 2013. 60(3): p. 691-699.
- [13] Chrobak, K.M., D.R. Potter, and J. Tien, Formation of perfused, functional microvascular tubes in vitro. Microvascular research, 2006. 71(3): p. 185-196.
- [14] Lee, W., et al., On demand three dimensional freeform fabrication of multi - layered hydrogel scaffold with fluidic channels. Biotechnology and bioengineering, 2010. 105(6): p. 1178-1186.
- [15] Ling, Y., et al., A cell-laden microfluidic hydrogel. Lab on a Chip, 2007. 7(6): p. 756-762.
- [16] Du, Y., et al., Sequential assembly of cell laden hydrogel constructs to engineer vascular - like microchannels. Biotechnology and bioengineering, 2011. 108(7): p. 1693-1703.
- [17] Zhang, Y., et al., Characterization of printable cellular micro-fluidic channels for tissue engineering. Biofabrication, 2013. 5(2): p. 025004.
- [18] Gao, Q., et al., Coaxial nozzle-assisted 3D bioprinting with built-in microchannels for nutrients delivery. Biomaterials, 2015. 61: p. 203-215.
- [19] Štumberger, G. and B. Vihar, Freeform perfusable microfluidics embedded in hydrogel matrices. Materials, 2018. 11(12): p. 2529.
- [20] Hinton, T.J., et al., Three-dimensional printing of complex biological structures by freeform reversible embedding of suspended hydrogels. Science advances, 2015. 1(9): p. e1500758.
- [21] Chen, Y., G.Z. Tan, and Y. Zhou, Effects of Viscosities and Solution Composition on Core-Sheath Electrospun Polycaprolactone (PCL) Nanoporous Microtubes. Polymers, 2021. 13(21): p. 3650.
- [22] Zhou, Y., D. Sooriyaarachchi, and G.Z. Tan, Fabrication of nanopores polylactic acid microtubes by core-sheath electrospinning for capillary vascularization. Biomimetics, 2021. 6(1): p. 15.
- [23] Zhou, Y. and G.Z. Tan, Core-sheath wet electrospinning of nanoporous polycaprolactone microtubes to mimic fenestrated capillaries. Macromolecular Materials and Engineering, 2020. 305(7): p. 2000180.
- [24] Arafa, E.G., et al., Eco-friendly and biodegradable sodium alginate/quaternized chitosan hydrogel for controlled release of urea and its antimicrobial activity. Carbohydr Polym, 2022. 291: p. 119555.
- [25] Lee, K.Y. and D.J. Mooney, Alginate: Properties and biomedical applications. Progress in Polymer Science, 2012. 37(1): p. 106-126.
- [26] Badita, C., et al., Characterization of sodium alginate based films. Rom. J. Phys, 2020. 65: p. 1-8.
- [27] Reed, A.M. and D.K. Gilding, Biodegradable polymers for use in surgery — poly(ethylene oxide)/poly(ethylene terephthalate) (PEO/PET) copolymers: 2. In vitro degradation. Polymer, 1981. 22(4): p. 499-504.
- [28] Rani, G.U. and S. Sharma, Biopolymers, Bioplastics and Biodegradability: An Introduction, in Encyclopedia of Materials: Plastics and Polymers, M.S.J. Hashmi, Editor. 2022, Elsevier: Oxford. p. 474-486.
- [29] Fattah-alhosseini, A., et al., A review of effective strides in amelioration of the biocompatibility of PEO coatings on Mg alloys. Journal of Magnesium and Alloys, 2022. 10(9): p. 2354-2383.
- [30] Archer, E., M. Torretti, and S. Madbouly, *Biodegradable polycaprolactone (PCL) based polymer and composites*. Physical Sciences Reviews, 2021(000010151520200074).
- [31] Cho, Y.I. and K.R. Kensey, Effects of the non-Newtonian viscosity of blood on flows in a diseased arterial vessel. Part 1: Steady flows. Biorheology, 1991. 28(3-4): p. 241-262.
- [32] Weddell, J.C., et al., Hemodynamic analysis in an idealized artery tree: differences in wall shear stress between Newtonian and non-Newtonian blood models. PloS one, 2015. 10(4): p. e0124575.
- [33] Stijnman, A.C., I. Bodnar, and R.H. Tromp, Electrospinning of food-grade polysaccharides. Food Hydrocolloids, 2011. 25(5): p. 1393-1398.
- [34] He, Y., et al., Research on the printability of hydrogels in 3D bioprinting. Scientific reports, 2016. 6(1): p. 1-13.
- [35] Naghieh, S. and X. Chen, Printability—A key issue in extrusion-based bioprinting. Journal of Pharmaceutical Analysis, 2021. 11(5): p. 564-579.

- [36] Lagar, J.H. and M.G.C. Raborar. Material contrast identification and compositional contrast mapping using back-scattered electron imaging. in Proceedings of the 20th IEEE International Symposium on the Physical and Failure Analysis of Integrated Circuits (IPFA). 2013. IEEE.
- [37] Haug, A. and O. Smidsrød, Strontium-calcium selectivity of alginates. Nature, 1967. 215(5102): p. 757-757.
- [38] Li, Y., et al., Advanced electrospun hydrogel fibers for wound healing. Composites Part B: Engineering, 2021. 223: p. 109101.
- [39] Han, N., et al., Hydrogel-electrospun fiber composite materials for hydrophilic protein release. Journal of controlled release, 2012. 158(1): p. 165-170
- [40] Teixeira, M.O., J.C. Antunes, and H.P. Felgueiras, Recent advances in fiber-hydrogel composites for wound healing and drug delivery systems. Antibiotics, 2021. 10(3): p. 248.
- [41] Laco, F., M.H. Grant, and R.A. Black, Collagen-nanofiber hydrogel composites promote contact guidance of human lymphatic microvascular endothelial cells and directed capillary tube formation. Journal of Biomedical Materials Research Part A, 2013. 101(6): p. 1787-1799.
- [42] Xu, S., et al., Composites of electrospun -fibers and hydrogels: a potential solution to current challenges in biological and biomedical field. Journal of Biomedical Materials Research Part B: Applied Biomaterials, 2016. 104(3): p. 640-656.
- [43] McMahon, R.E., et al., Hydrogel-electrospun mesh composites for coronary artery bypass grafts. Tissue Engineering Part C: Methods, 2011. 17(4): p. 451-461.
- [44] Yang, Y., I. Wimpenny, and M. Ahearne, Portable nanofiber meshes dictate cell orientation throughout three-dimensional hydrogels. Nanomedicine: Nanotechnology, Biology and Medicine, 2011. 7(2): p. 131-136.
- [45] Bosworth, L.A., L.-A. Turner, and S.H. Cartmell, State of the art composites comprising electrospun fibres coupled with hydrogels: a review. Nanomedicine: Nanotechnology, Biology and Medicine, 2013. 9(3): p. 322-335.
- [46] Khalil, S. and W. Sun, Bioprinting endothelial cells with alginate for 3D tissue constructs. 2009.
- [47] Nair, K., et al., Characterization of cell viability during bioprinting processes. Biotechnology Journal: Healthcare Nutrition Technology, 2009. 4(8): p. 1168-1177.
- [48] Xu, C., et al., Scaffold free inkjet printing of three dimensional zigzag cellular tubes. Biotechnology and bioengineering, 2012. 109(12): p. 3152-3160
- [49] Xu, C., et al., Study of droplet formation process during drop-on-demand inkjetting of living cell-laden bioink. Langmuir, 2014. 30(30): p. 9130-9138.
- [50] Chang, R., et al., Biofabrication of a three-dimensional liver micro-organ as an in vitro drug metabolism model. Biofabrication, 2010. 2(4): p. 045004.
- [51] Beckett, L.E., et al., Enhancement of the Mechanical Properties of Hydrogels with Continuous Fibrous Reinforcement. ACS Biomater Sci Eng, 2020. 6(10): p. 5453-5473.
- [52] Wu, S., et al., Living nano-micro fibrous woven fabric/hydrogel composite scaffolds for heart valve engineering. Acta biomaterialia, 2017. 51: p. 89-100
- [53] Sacks, M.S., Incorporation of Experimentally-Derived Fiber Orientation into a Structural Constitutive Model for Planar Collagenous Tissues. Journal of Biomechanical Engineering, 2003. 125(2): p. 280-287.
- [54] Jang, J., et al., Improving mechanical properties of alginate hydrogel by reinforcement with ethanol treated polycaprolactone nanofibers. Composites Part B: Engineering, 2013. 45(1): p. 1216-1221.
- [55] Padalhin, A.R., et al., Evaluation of the cytocompatibility hemocompatibility in vivo bone tissue regenerating capability of different PCL blends. Journal of Biomaterials Science, Polymer Edition, 2014. 25(5): p. 487-503
- [56] Nguyen, T.-H., et al., A hybrid electrospun PU/PCL scaffold satisfied the requirements of blood vessel prosthesis in terms of mechanical properties, pore size, and biocompatibility. Journal of Biomaterials Science, Polymer Edition, 2013. 24(14): p. 1692-1706.
- [57] Fakhrali, A., et al., Biocompatible graphene embedded PCL/PGS based nanofibrous scaffolds: A potential application for cardiac tissue regeneration. Journal of Applied Polymer Science, 2021. 138(40): p. 51177
- [58] Suntornnond, R., J. An, and C.K. Chua, Effect of gas plasma on polycaprolactone (PCL) membrane wettability and collagen type I immobilized for enhancing cell proliferation. Materials Letters, 2016. 171: p. 29